NANO LETTERS

pubs.acs.org/NanoLett Letter

Quantum Imaging of Magnetic Phase Transitions and Spin Fluctuations in Intrinsic Magnetic Topological Nanoflakes

Nathan J. McLaughlin, Chaowei Hu, Mengqi Huang, Shu Zhang, Hanyi Lu, Gerald Q. Yan, Hailong Wang, Yaroslav Tserkovnyak, Ni Ni, and Chunhui Rita Du*

Cite This: *Nano Lett.* 2022, 22, 5810–5817 Read Online

ACCESS | Metrics & More | Article Recommendations | Supporting Information

ABSTRACT: Topological materials featuring exotic band structures, unconventional current flow patterns, and emergent organizing principles offer attractive platforms for the development of next-generation transformative quantum electronic technologies. The family of $MnBi_2Te_4$ $(Bi_2Te_3)_n$ materials is naturally relevant in this context due to their nontrivial band topology, tunable magnetism, and recently discovered extraordinary quantum transport behaviors. Despite numerous pioneering studies to date, the local magnetic properties of $MnBi_2Te_4$ $(Bi_2Te_3)_n$ remain an open question, hindering a comprehensive understanding of their fundamental material properties. Exploiting nitrogen-vacancy (NV) centers in diamond, we report nanoscale quantum imaging of the magnetic phase transitions and spin fluctuations in exfoliated $MnBi_4Te_7$ flakes, revealing the underlying spin transport physics and magnetic domains at the nanoscale. Our results highlight the unique advantage of NV centers in exploring the magnetic properties of emergent quantum materials, opening new opportunities for investigating the interplay between topology and magnetism.

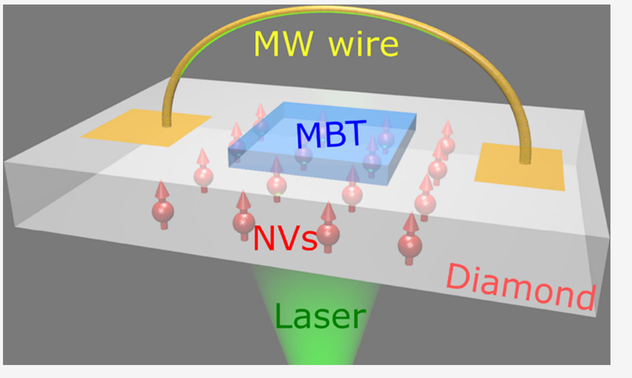

KEYWORDS: *Quantum sensing, Nitrogen vacancy magnetometry, Topological magnets, Spin fluctuations, Antiferromagnetic materials*

The interplay between magnetism and band topology promises to bring a plethora of exotic behaviors in emergent quantum materials, such as the quantum anomalous Hall effect,[1−6] surface ferromagnetism,[7−11] topological magnetoelectric effect,[12,13] and many others.[14−16] Over the past few years, the family of $MnBi_2Te_4$ $(Bi_2Te_3)_n$ materials has emerged as an attractive platform for exploring topologically dictated quantum spin and charge transport behaviors at relatively high temperatures.[4,17−26] The discovery and understanding of these emergent material properties of two-dimensional (2D) $MnBi_2Te_4$ $(Bi_2Te_3)_n$ materials relies on concurrent developments in theory, material synthesis, and sensitive metrology tools capable of characterizing local magnetic properties at the nanoscale, which remains a formidable challenge given the current state of the art. The major difficulty results from the significantly reduced magnetic flux generated by the weak or nearly compensated magnetic moment of 2D $MnBi_2Te_4$ $(Bi_2Te_3)_n$ samples, which is beyond the detection limit of most conventional magnetometry techniques. While some methods such as magneto-optic-Kerr-effect microscopy,[27] reflective magnetic circular dichroism,[17] and Raman spectroscopy[28,29] could be employed to qualitatively diagnose the magnetic states of 2D $MnBi_2Te_4$ $(Bi_2Te_3)_n$ flakes, these techniques provide limited quantitative information about local magnetization, and the field sensitivity of these tools is often compromised by interference effects and constrained by the optical diffraction limit.

To address this challenge we introduce nitrogen-vacancy (NV) centers, optically active atomic defects in diamond that act as single-spin sensors,[30−32] to perform nanoscale quantum imaging of $MnBi_4Te_7$ nanoflakes. By performing spatially resolved NV wide-field magnetometry measurements,[33−36] we directly image the local magnetization of $MnBi_4Te_7$ nanoflakes and the characteristic multidomain evolution behavior in a first-order magnetic transition process. Using NV relaxometry methods,[37−41] we have observed spatially varied dynamic magnetic fluctuations in $MnBi_4Te_7$, revealing the underlying spin transport physics and the low-frequency spin dynamics hosted by domain walls in these magnetic materials. We expect that the presented NV quantum sensing platform can be readily extended to a large family of layered van der Waals crystals,[31,42,43] providing ample opportunities for investigating

Received: April 6, 2022
Revised: July 6, 2022
Published: July 11, 2022

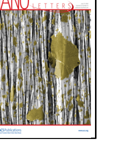

https://doi.org/10.1021/acs.nanolett.2c01390
Nano Lett. 2022, 22, 5810−5817

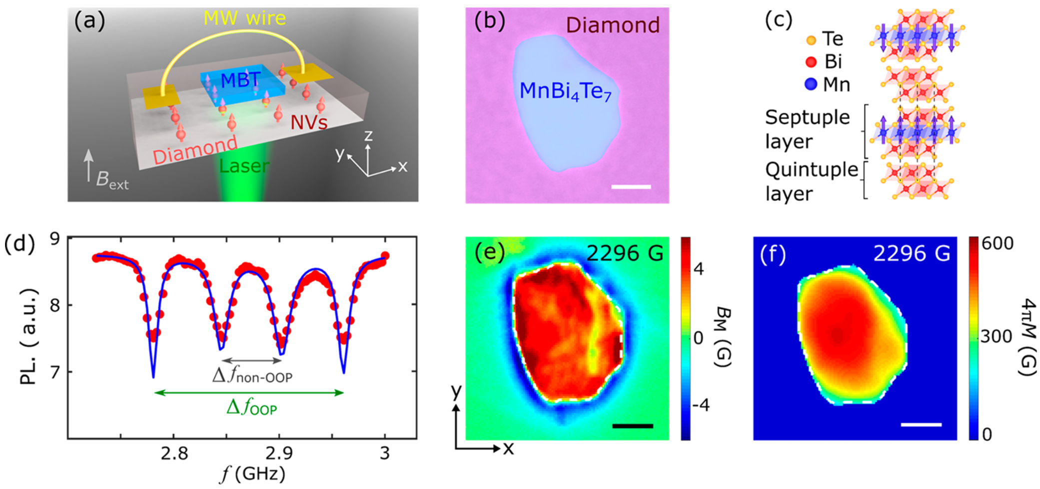

Figure 1. (a) Schematic of an exfoliated $MnBi_4Te_7$ flake transferred onto a [111] oriented diamond membrane for nitrogen-vacancy (NV) wide-field magnetometry measurements. (b) Optical image of a prepared diamond-$MnBi_4Te_7$ device. (c) Schematic of the crystal and magnetic structures of $MnBi_4Te_7$. (d) Optically detected magnetic resonance spectrum of NV centers contained in [111] oriented diamond with an external field B_{ext} applied along the out-of-plane (OOP) direction. The experimental spectrum is comprised of two pairs of resonance peaks corresponding to the Zeeman splitting of NV spins with OOP orientation and NV spins aligned along other directions (non-OOP). (e,f) Two-dimensional images of static stray field B_M (e) and reconstructed magnetization $4\pi M$ (f) of the exfoliated $MnBi_4Te_7$ flake measured at 4.5 K with B_{ext} = 2296 G. The white dashed lines mark the boundary of the exfoliated $MnBi_4Te_7$ flake, and the scale bar is 4 μm in panels b, e, and f.

the local spin dynamics and transport behaviors in a broad range of quantum materials.[41,44−46]

Figure 1a shows a schematic of our measurement platform, in which a [111] oriented diamond sample[47] containing shallowly implanted NV ensembles is used for the quantum sensing measurements. Note that one of the four possible NV orientations is along the out-of-plane direction (z axis), serving as an ideal local sensor to investigate the magnetic dynamics and phase transition of $MnBi_4Te_7$ with spontaneous perpendicular anisotropy. An 83 nm thick exfoliated $MnBi_4Te_7$ flake with lateral dimensions of approximately ~10 × 14 μm^2 is transferred onto the diamond surface, as shown in Figure 1b (see Supporting Information Section 1). Figure 1c illustrates the crystal and magnetic structure of $MnBi_4Te_7$, where the magnetic septuple layer ($MnBi_2Te_4$) and the nonmagnetic quintuple layer (Bi_2Te_3) stack alternately.[48] In the magnetic ground state, moments carried by the Mn^{2+} ions in individual septuple layers align parallel with each other along the out-of-plane direction due to the dominant intralayer ferromagnetic exchange interaction. Neighboring septuple layers are anti-ferromagnetically coupled, but can be driven into a ferromagnetic configuration by applying a sufficiently strong external perpendicular magnetic field B_{ext}.

We first utilize NV spin sensors to image the field-driven antiferromagnetic-to-ferromagnetic phase transition of the exfoliated $MnBi_4Te_7$ flake. The dc NV wide-field magnetometry measurements exploit the Zeeman splitting effect of the NV S = 1 electron spins to measure the local magnetic field along the NV-axis.[30,31] Figure 1d shows an example of the measured NV ESR spectrum, which exhibits two pairs of Zeeman split NV spin energy levels. The outer pair corresponds to NV centers with the out-of-plane (OOP) orientation, whereas the inner pair is degenerate and corresponds to NV centers with axes along the other three possible directions.[47] The magnitude of the local static magnetic field B_{tot} can be extracted as $B_{tot} = \pi\Delta f_{OOP}/\tilde{\gamma}$, where Δf_{OOP} characterizes the Zeeman splitting of the OOP-oriented NVs, and $\tilde{\gamma}$ is the gyromagnetic ratio of the NV centers. Subtracting the contribution from the external magnetic field B_{ext}, the magnetic stray field B_M generated from the $MnBi_4Te_7$ flake can be quantitatively measured. By performing spatially dependent optically detected magnetic resonance (ODMR) measurements over the NV ensembles, we can obtain a 2D stray field map as illustrated in Figure 1e, which is measured at a temperature T = 4.5 K and B_{ext} = 2296 G. Through established reverse-propagation protocols[31,34] (see Supporting Information Section 2), the corresponding magnetization ($4\pi M$) map of the exfoliated $MnBi_4Te_7$ flake can be quantitatively extracted, as shown in Figure 1f.

To directly image the first-order magnetic phase transition, Figure 2a−f presents the obtained 2D magnetization maps of the $MnBi_4Te_7$ flake measured with an increasing perpendicular magnetic field B_{ext}. In the low-field regime (B_{ext} < 1000 G), the exfoliated MnBi4Te7 flake exhibits a vanishingly small net magnetic moment, as shown in Figure 2a,b, due to the antiferromagnetic coupling between the neighboring magnetic septuple layers. A finite magnetic moment shown in the top left region of the flake results from field induced polarization. When B_{ext} increases to 1220 G, the characteristic spin flip transition propagates from the top left area of the flake, leading to a "partial" ferromagnetic state with enhanced local magnetization. Such a "partial" ferromagnetic phase features a coexistence of ferromagnetic and antiferromagnetic ordering of septuple layers along the out-of-plane direction due to the weak interlayer exchange coupling. Note that the remaining area of the $MnBi_4Te_7$ flake stays in the antiferromagnetic ground state with the formation of incipient magnetic domain walls at locations with the lowest energy barrier, as shown in Figure 2c. The observed spin flip transition expands to the entire $MnBi_4Te_7$ flake through domain wall propagation with increasing perpendicular field [Figure 2d,e] and the local magnetization further increases as the individual magnetic septuple layers become fully aligned. When B_{ext} >2000 G, this magnetic phase transition concludes with a saturated local magnetization, as shown in Figure 2f. The variation of the local magnetization of the $MnBi_4Te_7$ flake may result from

https://doi.org/10.1021/acs.nanolett.2c01390
Nano Lett. 2022, 22, 5810−5817

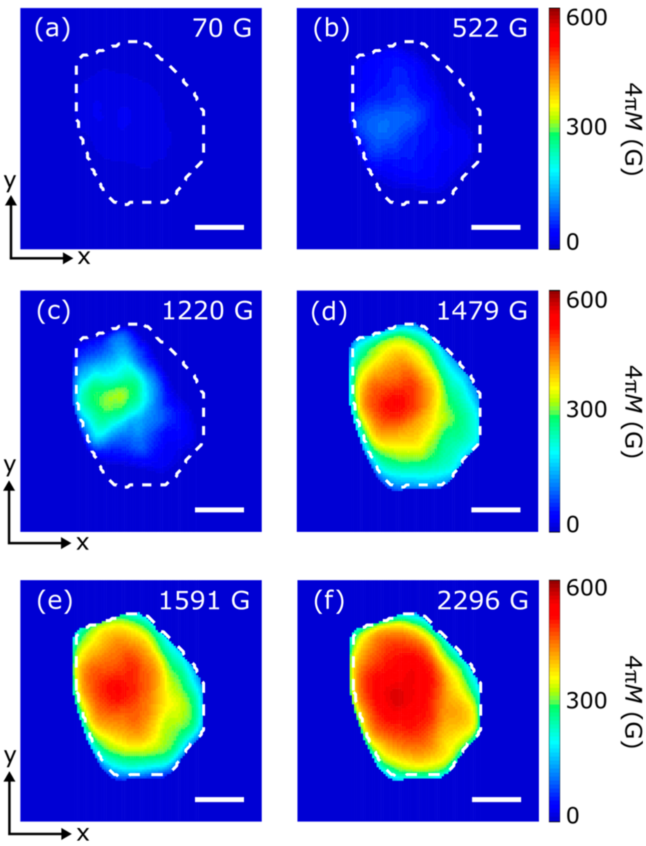

Figure 2. (a−f) Reconstructed magnetization ($4\pi M$) maps of an $MnBi_4Te_7$ flake measured at 4.5 K and B_{ext} = 70 G (a), 522 G (b), 1220 G (c), 1479 G (d), 1591 G (e), and 2296 G (f), respectively. The white dashed lines mark the boundary of the exfoliated flake, and the scale bar is 4 μm.

inhomogeneities,[49] magnetic domains,[27,50] and localized defects.[51] The presented results highlight a spatially nonuniform spin flip transition process of the 2D $MnBi_4Te_7$ flake at the nanoscale, exhibiting magnetic domain nucleation and domain wall propagation behaviors.

As qubit-based magnetometers, NV centers possess excellent quantum coherence,[30] providing opportunities for probing fluctuating magnetic fields that are challenging to access by conventional magnetometry methods.[37,38,40,41] Next, we apply NV wide-field magnetometry to directly measure dynamic magnetic fluctuations in an exfoliated $MnBi_4Te_7$ flake, from which the underlying spin transport physics and the low-frequency spin dynamics hosted by magnetic domain walls in this magnetic topological material can be revealed. Figure 3a shows the dispersion of bulk $MnBi_4Te_7$ with an energy gap of ∼51 GHz (see Supporting Information Section 3). At thermal equilibrium, fluctuations of the transverse and longitudinal spin density of $MnBi_4Te_7$ generate fluctuating stray fields, as illustrated in Figure 3b. Microscopically, the transverse spin fluctuations vanish below the magnon band minimum and are related to single magnon processes.[41,52] The longitudinal spin fluctuations are related to two-magnon processes,[39,45,46] where a magnon with frequency f is scattered to another one with frequency $f \pm f_{2m}$, emitting (absorbing) magnetic noise at frequency f_{2m}.

Experimentally, we used NV relaxometry techniques to detect the fluctuating magnetic fields generated by spin fluctuations in the $MnBi_4Te_7$ flake. The top panel of Figure 3c shows the optical and microwave measurement sequence. A green laser pulse first initializes the NV spin to the $m_s = 0$ state. Spin fluctuations in the $MnBi_4Te_7$ sample couple to proximate NV centers through the dipole−dipole interaction. Fluctuating magnetic fields at the NV ESR frequencies induce NV spin transitions from the $m_s = 0$ to the $m_s = \pm 1$ states, leading to an enhancement of the NV relaxation rate Γ.[37−41] After a delay time t, we measure the occupation probabilities of the NV spin

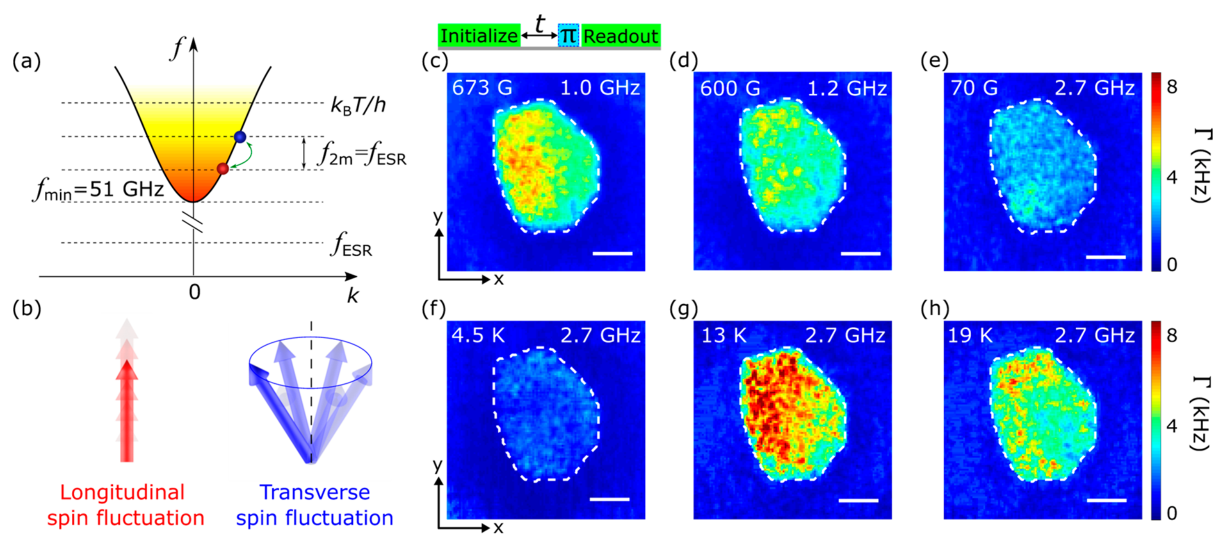

Figure 3. (a) Sketch of the magnon dispersion of bulk $MnBi_4Te_7$. The magnon occupation follows the Bose−Einstein distribution as indicated by the fading colors. The minimal magnon frequency f_{min} is ∼51 GHz, which is much larger than the NV electron spin resonance frequencies f_{ESR} in our measured field range. The longitudinal spin fluctuations with a characteristic frequency of f_{2m} are associated with two-magnon scattering processes and couple with a NV center through dipolar interactions. (b) Schematic of the dynamic fluctuations of the longitudinal and transverse spin density. (c−e) NV spin relaxation maps measured at f_{ESR} of 1.0 GHz (c), 1.2 GHz (d), and 2.7 GHz (e) at 8.5 K. Top panel of (c): optical and microwave sequence of NV relaxometry measurements. (f−h) NV spin relaxation maps measured at 4.5 K (f), 13 K (g), and 19 K (h) with f_{ESR} = 2.7 GHz. The white dashed lines mark the boundary of the exfoliated flake, and scale bar is 4 μm in panels c−h.

https://doi.org/10.1021/acs.nanolett.2c01390
Nano Lett. 2022, 22, 5810−5817

in the $m_s = 0$ and the $m_s = \pm 1$ states by applying a microwave π-pulse at the corresponding ESR frequencies and measuring the spin-dependent photoluminescence via a green-laser readout pulse.[53] By measuring the integrated photoluminescence intensity as a function of the delay time t and fitting the data with a three-level model,[41,52] the NV relaxation rates can be quantitatively obtained (see Supporting Information Section 4). We highlight that in the low-field regime with a quasi-uniform magnetic domain structure, the NV ESR frequencies in our measurements are much lower than the minimum magnon energy of $MnBi_4Te_7$. Thus, the measured NV relaxation is driven primarily by longitudinal spin fluctuations. In contrast, in the high-field regime where multidomains form during the spin flip transition of $MnBi_4Te_7$, the magnetic noise generated by the low-frequency spin dynamics hosted by magnetic domain walls[40,54] also plays a role.

We focus our NV relaxometry measurements in the low-field regime to detect the longitudinal spin fluctuations of the $MnBi_4Te_7$ nanoflake. Figure 3c−e shows the 2D maps of the measured NV relaxation rate at 8.5 K at ESR frequencies of 1.0, 1.2, and 2.7 GHz, respectively. The applied perpendicular magnetic field B_{ext} is below 800 G to ensure a quasi-single magnetic domain feature of the sample. Notably, the measured NV spin relaxation rate Γ is significantly enhanced in the diamond area covered by the $MnBi_4Te_7$ flake. The magnitude of Γ decreases with increasing NV ESR frequency, suggesting that a larger energy difference invoked in the two-magnon process discussed above suppresses longitudinal spin fluctuations, in qualitative agreement with our theoretical model (see Supporting Information Section 5).[45,46] Figure 3f−h shows the 2D NV relaxation maps measured at an ESR frequency of 2.7 GHz at 4.5, 13, and 19 K, respectively. When T = 4.5 K, the magnetic fluctuations are suppressed due to the reduced thermal magnon energy, leading to negligible NV spin relaxation. Notably, we observed significantly enhanced longitudinal spin fluctuations at a temperature of 13 K, which is expected due to the increase in the magnetic susceptibility of $MnBi_4Te_7$ around the Néel temperature T_N.[48] When T = 19 K, longitudinal spin fluctuations remain, which is attributed to the finite spin−spin correlation in the paramagnetic state.[55] The observed spatially varying magnetic fluctuations over the exfoliated $MnBi_4Te_7$ flake could be induced by inhomogeneities in magnetic susceptibility, spin diffusion constant, and exchange coupling strength.

The measured NV relaxation rate driven by longitudinal spin fluctuations at the NV ESR frequency f_{ESR} is related by the fluctuation−dissipation theorem to the dynamic spin susceptibility χ'' of the $MnBi_4Te_7$ sample and the NV transfer function in the high temperature limit as follows[45,46]

$$\Gamma(f_{ESR}) = \frac{(\gamma\tilde{\gamma})^2 k_B T}{2\pi f_{ESR}} \int \mathcal{F}(\mathbf{k}, d)\chi''(\mathbf{k}, D)\mathrm{d}\mathbf{k} + \Gamma^0 \tag{1}$$

where the first term on the right represents the NV relaxation rate Γ^M induced by spin dynamics of the $MnBi_4Te_7$ flake and Γ^0 is the intrinsic NV relaxation rate that is independent of the spin dynamics of $MnBi_4Te_7$. γ and $\tilde{\gamma}$ are the gyromagnetic ratio of the magnetic sample and NV centers, k_B is the Boltzmann constant, T is temperature, $\mathbf{k}$ is the magnon wavevector, $\mathcal{F}(\boldsymbol{k},d)$ is the transfer function[52] describing the magnetic fields generated at the NV site, and d is the NV-to-sample distance. The dynamic spin susceptibility χ'' reflects underlying spin transport properties of a magnetic sample, which can be expressed as a function of the intrinsic spin diffusion constant D and the static longitudinal magnetic susceptibility per layer χ_0 via the conventional diffusion equation[46,56] (see Supporting Information Section 5). By measuring the NV relaxation rate as a function of ESR frequency, we can extract the key material parameters D and χ_0 of the $MnBi_4Te_7$ flake. Figure 4a plots a

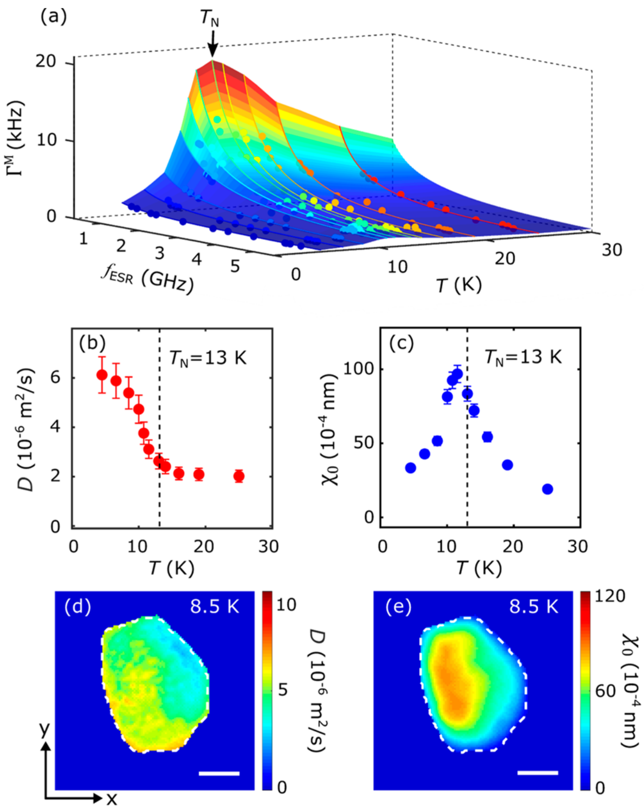

Figure 4. (a) NV relaxation rates Γ^M measured as a function of temperature and the NV electron spin resonance frequency f_{ESR}, from which the spin diffusion constant and magnetic susceptibility per layer can be extracted. The solid lines are fitting curves to the theoretical calculation. (b) Intrinsic spin diffusion constant D measured as a function of temperature. (c) Temperature dependence of the obtained longitudinal static magnetic susceptibility χ_0. (d,e) Two-dimensional images of D and χ_0 of the $MnBi_4Te_7$ flake at 8.5 K. The white dashed lines mark the boundary of the exfoliated flake, and the scale bar is 4 μm.

three-dimensional map of the spatially averaged NV relaxation rates Γ^M of the flake as a function of ESR frequency and temperature. The variation of the NV relaxation rate agrees well with the theoretical model of eq 1 from which the intrinsic spin diffusion constant D and the static longitudinal magnetic susceptibility χ_0 of $MnBi_4Te_7$ at individual temperatures can be extracted, as presented in Figure 4b−c. D is obtained to be $(6.1 \pm 0.8) \times 10^{-6}$ m/s^2 at 4.5 K, in qualitative agreement with the theoretical estimation of $D = \upsilon^2\tau/2$[57] when taking the magnon velocity to be $\upsilon \sim 1$ km/s[48] and the momentum scattering time $\tau \sim 10$ ps. Below the Néel temperature (~13 K) of $MnBi_4Te_7$, D monotonically decreases as the temperature increases due to a reduction of τ caused by enhanced Umklapp scattering.[58] When T > 14 K, D decays to an approximately constant value and the residual spin transport capability results from atomic scale thermal spin fluctuations. The obtained static magnetic susceptibility χ_0 generally agrees with previous measurements

https://doi.org/10.1021/acs.nanolett.2c01390
Nano Lett. 2022, 22, 5810−5817

of bulk $MnBi_4Te_7$ samples.[48] As shown in Figure 4c, χ_0 reaches a peak value of $(9.9 \pm 0.6) \times 10^{-3}$ nm around the Néel temperature of $MnBi_4Te_7$, which is consistent with the antiferromagnetic phase transition.[48] Figure 4d,e shows the obtained 2D maps of spin diffusion constant D and static magnetic susceptibility χ_0 of the exfoliated $MnBi_4Te_7$ flake, respectively, measured at 8.5 K. Note that the enhanced χ_0 in the top left region of the flake is consistent with the observed larger field-induced magnetic moment, as shown in Figure 2a,b.

Next, we move to the high-field regime to image spin fluctuations generated by magnetic domain walls in an $MnBi_4Te_7$ flake during the spin flip transition. In magnetic topological materials, domain walls serve as intrinsic boundaries between two topological states with opposite chiralities.[15,59] Because the Chern number must change discontinuously across neighboring magnetic domains, chiral edge states are expected to reside along domain walls, offering an attractive platform to realize and engineer exotic quantum spin and charge transport behaviors.[15,59] Figure 5a illustrates the evolution of magnetic phases of $MnBi_4Te_7$ as a function of increasing perpendicular magnetic field B_{ext}. In the antiferromagnetic and ferromagnetic states, the magnetization of each septuple layer is uniformly aligned and the bulk spin excitation energy of $MnBi_4Te_7$ is larger than the NV ESR frequencies in the accessible magnetic field range due to the large magnetic anisotropy. In this case, the NV-magnon coupling is mediated by longitudinal spin fluctuations as discussed above. During the spin flip transition, spins in individual septuple layers may flip mostly independently due to weak interlayer coupling. Nucleation of domain walls occurs at locations within of an exfoliated $MnBi_4Te_7$ flake where the energy barrier is the lowest and form partially magnetically flipped septuple layers, as illustrated in the middle panel of Figure 5a. The low-frequency spin dynamics hosted by magnetic domain walls will generate fluctuating magnetic stray fields,[40,54] driving NV relaxation at the corresponding ESR energy.

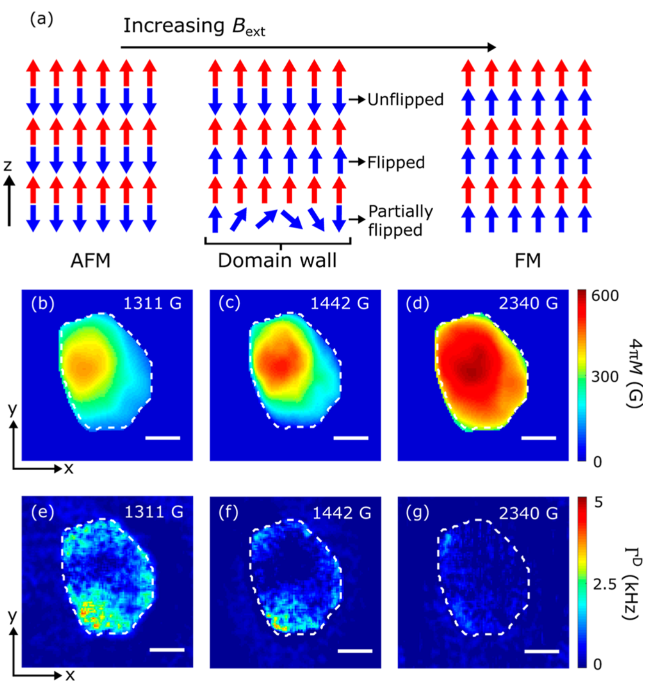

Figure 5. (a) Schematic of the evolution of the magnetic states of $MnBi_4Te_7$ as a function of increasing perpendicular magnetic field B_{ext}. In the ferromagnetic and antiferromagnetic phases, the magnetic moments of individual magnetic septuple layers are fully aligned parallel or antiparallel without the formation of magnetic domains. During the spin flip transition process, spins in individual septuple layers could flip mostly independently. Magnetic domain walls nucleate at locations where the energy barrier is lowest, leading to a magnetic gradient in the lateral direction of a partially flipped septuple layer. (b−d) Reconstructed magnetization maps of the $MnBi_4Te_7$ flake measured at B_{ext} of 1311 G (b), 1442 G (c), and 2340 G (d). (e−g) Magnetic domain wall-induced NV spin relaxation maps measured at the corresponding magnetic fields. The longitudinal spin noise generated from the bulk spin excitations has been subtracted to highlight the contribution Γ^D from the magnetic domain walls. The white dashed lines mark the boundary of the exfoliated flake, and the scale bar is 4 μm in panels b−g.

Figure 5b−d shows NV wide-field static magnetization images of the $MnBi_4Te_7$ flake measured at 1311, 1442, and 2340 G, respectively. An applied perpendicular magnetic field B_{ext} induces the formation of magnetic domains during the spin flip transition [Figure 5b,c]. Figure 5e−g shows 2D maps of the NV relaxation rate measured at the corresponding magnetic fields. Note that the background of the NV relaxation rate induced by longitudinal spin noise generated from bulk spin excitations has been subtracted to highlight the contribution Γ^D from the spin fluctuations in magnetic domain walls. (See Supporting Information Section 6 for details.) When B_{ext} = 1311 G, the top-left corner of the $MnBi_4Te_7$ flake becomes polarized while the rest of the sample remains partially magnetically flipped. This is accompanied by the formation of lateral magnetic domain walls that generate significantly enhanced magnetic noise. Note that the flipped area of the $MnBi_4Te_7$ flake expands when increasing B_{ext} to 1422 G and suppresses the NV relaxation rate, as shown in Figure 5f. When B_{ext} = 2340 G, $MnBi_4Te_7$ enters the fully saturated ferromagnetic state shown in Figure 5d, and generates a vanishingly small spin noise Γ^D due to the absence of magnetic domain walls. Qualitatively, the measured NV relaxation rate increases with the domain wall density, which is further related to the gradient of the magnetization (see Supporting Information Section 7 for details).

Direct imaging of magnetic domain walls in intrinsic magnetic topological materials could provide an opportunity to investigate the interplay between local magnetization and macroscopic quantum transport behaviors, for example, the high-temperature quantum anomalous Hall effect[4−6,16] and layer Hall effect[18] recently discovered in $MnBi_2Te_4\,(Bi_2Te_3)_n$. The spatial resolution of the presented NV wide-field imaging technique lies at the optical diffraction limit of ∼500 nm. By employing scanning NV microscopy methods,[31,32,40,42] we expect the spatial resolution to ultimately reach the tens of nanometers regime, offering new opportunities to uncover detailed microscopic features of magnetic patterns in quantum materials.

In summary, we have used NV centers as a nanoscale local probe to investigate magnetic phase transitions and spin fluctuations in magnetic topological materials. The spatially resolved NV magnetometry measurements reveal characteristic domain wall nucleation and propagation features during the spin flip transition of $MnBi_4Te_7$ flakes. By employing NV relaxometry techniques, we access the longitudinal spin fluctuations in $MnBi_4Te_7$, from which the intrinsic spin diffusion constant and static magnetic susceptibility are

https://doi.org/10.1021/acs.nanolett.2c01390
Nano Lett. 2022, 22, 5810−5817

obtained. We also observe a dramatic increase of magnetic noise arising from magnetic domain walls in an $MnBi_4Te_7$ flake, which is attributed to low-frequency spin fluctuations hosted by spatially evolving magnetic textures. Because magnetic domain walls and spin fluctuations are fundamentally related to mesoscopic spin and charge transport in topological materials, nanoscale imaging of relevant material parameters will contribute to a comprehensive understanding of the exotic properties of the family of $MnBi_2Te_4$ $(Bi_2Te_3)_n$ materials (See Supporting Information Section 8 for details). Our results further illustrate the capabilities of NV centers in probing the nanoscale spin transport and dynamics in emergent condensed matter systems, opening new possibilities for investigating the interplay between magnetism and topology in a broad range of low-dimensional materials. The dynamic coupling between topological materials and NV spin qubits may also point to the possibility of developing NV-based hybrid architectures for next-generation quantum information sciences and technologies.[54]

ASSOCIATED CONTENT

Supporting Information

The Supporting Information is available free of charge at https://pubs.acs.org/doi/10.1021/acs.nanolett.2c01390.

Details on materials and methods; spinwave dispersion calculation; numerical analysis of NV results to extract magnetization, magnetic constants, relaxation rates, and domain wall density; additional measurements on other members of family of $MnBi_2Te_4$ $(Bi_2Te_3)_n$ materials (PDF)

AUTHOR INFORMATION

Corresponding Author

Chunhui Rita Du – *Department of Physics, University of California, La Jolla, California 92093, United States; Center for Memory and Recording Research, University of California, La Jolla, California 92093, United States;* orcid.org/0000-0001-8063-7711; Email: c1du@physics.ucsd.edu

Authors

Nathan J. McLaughlin – *Department of Physics, University of California, La Jolla, California 92093, United States*

Chaowei Hu – *Department of Physics and Astronomy, University of California, Los Angeles, California 90095, United States*

Mengqi Huang – *Department of Physics, University of California, La Jolla, California 92093, United States*

Shu Zhang – *Department of Physics and Astronomy, University of California, Los Angeles, California 90095, United States*

Hanyi Lu – *Department of Physics, University of California, La Jolla, California 92093, United States*

Gerald Q. Yan – *Department of Physics, University of California, La Jolla, California 92093, United States;* orcid.org/0000-0002-8011-0941

Hailong Wang – *Center for Memory and Recording Research, University of California, La Jolla, California 92093, United States*

Yaroslav Tserkovnyak – *Department of Physics and Astronomy, University of California, Los Angeles, California 90095, United States*

Ni Ni – *Department of Physics and Astronomy, University of California, Los Angeles, California 90095, United States*

Complete contact information is available at: https://pubs.acs.org/10.1021/acs.nanolett.2c01390

Notes

The authors declare no competing financial interest.

ACKNOWLEDGMENTS

Authors would like to thank Eric E. Fullerton for providing the Physical Property Measurement System for the electrical transport measurements and Yuxuan Xiao and Eric Lee-Wong for assistance in sample preparation and magnetometry characterization. Authors thank Yu-Hang Li, Ran Cheng, Yi-Zhuang You, Suyang Xu, Sheng-Chin Ho, and Anyuan Gao for insightful discussions. N.J.M., H.L., H.W., and C.H.R.D. were supported by the Air Force Office of Scientific Research under award FA9550-20-1-0319 and its Young Investigator Program under award FA9550-21-1-0125. M.H., G.Q.Y., and C.H.R.D. acknowledged the support from U.S. National Science Foundation (NSF) under award ECCS-2029558 and DMR-2046227. C.H. and N.N. were supported by the U.S. Department of Energy (DOE), Office of Science, Office of Basic Energy Sciences under Award No. DE-SC0021117 for the bulk single crystal growth and characterization. S.Z. and Y.T. were supported by NSF under Grant DMR-2049979.

REFERENCES

(1) Chang, C.-Z.; Zhang, J.; Feng, X.; Shen, J.; Zhang, Z.; Guo, M.; Li, K.; Ou, Y.; Wei, P.; Wang, L.-L.; Ji, Z.-Q.; Feng, Y.; Ji, S.; Chen, X.; Jia, J.; Dai, X.; Fang, Z.; Zhang, S.-C.; He, K.; Wang, Y.; Lu, L.; Ma, X.-C.; Xue, Q.-K. Experimental Observation of the Quantum Anomalous Hall Effect in a Magnetic Topological Insulator. *Science* **2013**, *340*, 167–170.

(2) Checkelsky, J. G.; Yoshimi, R.; Tsukazaki, A.; Takahashi, K. S.; Kozuka, Y.; Falson, J.; Kawasaki, M.; Tokura, Y. Trajectory of the Anomalous Hall Effect towards the Quantized State in a Ferromagnetic Topological Insulator. *Nat. Phys.* **2014**, *10*, 731–736.

(3) Kou, X.; Guo, S.-T.; Fan, Y.; Pan, L.; Lang, M.; Jiang, Y.; Shao, Q.; Nie, T.; Murata, K.; Tang, J.; Wang, Y.; He, L.; Lee, T.-K.; Lee, W.-L.; Wang, K. L. Scale-Invariant Quantum Anomalous Hall Effect in Magnetic Topological Insulators beyond the Two-Dimensional Limit. *Phys. Rev. Lett.* **2014**, *113*, 137201.

(4) Deng, Y.; Yu, Y.; Shi, M. Z.; Guo, Z.; Xu, Z.; Wang, J.; Chen, X. H.; Zhang, Y. Quantum Anomalous Hall Effect in Intrinsic Magnetic Topological Insulator $MnBi_2Te_4$. *Science* **2020**, *367*, 895–900.

(5) Serlin, M.; Tschirhart, C. L.; Polshyn, H.; Zhang, Y.; Zhu, J.; Watanabe, K.; Taniguchi, T.; Balents, L.; Young, A. F. Intrinsic Quantized Anomalous Hall Effect in a Moiré Heterostructure. *Science* **2020**, *367*, 900–903.

(6) Li, T.; Jiang, S.; Shen, B.; Zhang, Y.; Li, L.; Tao, Z.; Devakul, T.; Watanabe, K.; Taniguchi, T.; Fu, L.; Shan, J.; Mak, K. F. Quantum Anomalous Hall Effect from Intertwined Moiré Bands; *Nature* **2021**, *600*, 641–646.

(7) Nevola, D.; Li, H. X.; Yan, J.-Q.; Moore, R. G.; Lee, H.-N.; Miao, H.; Johnson, P. D. Coexistence of Surface Ferromagnetism and a Gapless Topological State in $MnBi_2Te_4$. *Phys. Rev. Lett.* **2020**, *125*, 117205.

(8) Mogi, M.; Yasuda, K.; Fujimura, R.; Yoshimi, R.; Ogawa, N.; Tsukazaki, A.; Kawamura, M.; Takahashi, K. S.; Kawasaki, M.; Tokura, Y. Current-Induced Switching of Proximity-Induced Ferromagnetic Surface States in a Topological Insulator. *Nat. Commun.* **2021**, *12*, 1404.

(9) Katmis, F.; Lauter, V.; Nogueira, F. S.; Assaf, B. A.; Jamer, M. E.; Wei, P.; Satpati, B.; Freeland, J. W.; Eremin, I.; Heiman, D.; Jarillo-Herrero, P.; Moodera, J. S. A High-Temperature Ferromagnetic

Topological Insulating Phase by Proximity Coupling. *Nature* **2016**, *533*, 513−516.
(10) Figueroa, A. I.; Bonell, F.; Cuxart, M. G.; Valvidares, M.; Gargiani, P.; van der Laan, G.; Mugarza, A.; Valenzuela, S. O. Absence of Magnetic Proximity Effect at the Interface of Bi_2Se_3 and $(Bi,Sb)_2Te_3$ with EuS. *Phys. Rev. Lett.* **2020**, *125*, 226801.
(11) Fijalkowski, K. M.; Hartl, M.; Winnerlein, M.; Mandal, P.; Schreyeck, S.; Brunner, K.; Gould, C.; Molenkamp, L. W. Coexistence of Surface and Bulk Ferromagnetism Mimics Skyrmion Hall Effect in a Topological Insulator. *Phys. Rev. X* **2020**, *10*, 011012.
(12) Xiao, D.; Jiang, J.; Shin, J. H.; Wang, W.; Wang, F.; Zhao, Y. F.; Liu, C.; Wu, W.; Chan, M. H. W.; Samarth, N.; Chang, C. Z. Realization of the Axion Insulator State in Quantum Anomalous Hall Sandwich Heterostructures. *Phys. Rev. Lett.* **2018**, *120*, 056801.
(13) Dziom, V.; Shuvaev, A.; Pimenov, A.; Astakhov, G. V.; Ames, C.; Bendias, K.; Böttcher, J.; Tkachov, G.; Hankiewicz, E. M.; Brüne, C.; Buhmann, H.; Molenkamp, L. W. Observation of the Universal Magnetoelectric Effect in a 3D Topological Insulator. *Nat. Commun.* **2017**, *8*, 1−8.
(14) Tsai, H.; Higo, T.; Kondou, K.; Nomoto, T.; Sakai, A.; Kobayashi, A.; Nakano, T.; Yakushiji, K.; Arita, R.; Miwa, S.; Otani, Y.; Nakatsuji, S. Electrical Manipulation of a Topological Antiferromagnetic State. *Nature* **2020**, *580*, 608−613.
(15) Yasuda, K.; Mogi, M.; Yoshimi, R.; Tsukazaki, A.; Takahashi, K. S.; Kawasaki, M.; Kagawa, F.; Tokura, Y. Quantized Chiral Edge Conduction on Domain Walls of a Magnetic Topological Insulator. *Science* **2017**, *358*, 1311−1314.
(16) Li, Y.-H.; Cheng, R. Spin Fluctuations in Quantized Transport of Magnetic Topological Insulators. *Phys. Rev. Lett.* **2021**, *126*, 026601.
(17) Ovchinnikov, D.; Huang, X.; Lin, Z.; Fei, Z.; Cai, J.; Song, T.; He, M.; Jiang, Q.; Wang, C.; Li, H.; Wang, Y.; Wu, Y.; Xiao, D.; Chu, J.-H.; Yan, J.; Chang, C.-Z.; Cui, Y.-T.; Xu, X. Intertwined Topological and Magnetic Orders in Atomically Thin Chern Insulator $MnBi_2Te_4$. *Nano Lett.* **2021**, *21*, 2544−2550.
(18) Gao, A.; Liu, Y.-F.; Hu, C.; Qiu, J.-X.; Tzschaschel, C.; Ghosh, B.; Ho, S.-C.; Bérubé, D.; Chen, R.; Sun, H.; Zhang, Z.; Zhang, X.-Y.; Wang, Y.-X.; Wang, N.; Huang, Z.; Felser, C.; Agarwal, A.; Ding, T.; Tien, H.-J.; Akey, A.; Gardener, J.; Singh, B.; Watanabe, K.; Taniguchi, T.; Burch, K. S.; Bell, D. C.; Zhou, B. B.; Gao, W.; Lu, H.-Z.; Bansil, A.; Lin, H.; Chang, T.-R.; Fu, L.; Ma, Q.; Ni, N.; Xu, S.-Y. Layer Hall Effect in a 2D Topological Axion Antiferromagnet. *Nature* **2021**, *595*, 521−525.
(19) Zhao, Y.-F.; Zhou, L.-J.; Wang, F.; Wang, G.; Song, T.; Ovchinnikov, D.; Yi, H.; Mei, R.; Wang, K.; Chan, M. H. W.; Liu, C.-X.; Xu, X.; Chang, C.-Z. Even-Odd Layer-Dependent Anomalous Hall Effect in Topological Magnet $MnBi_2Te_4$ Thin Films. *Nano Lett.* **2021**, *21*, 7691−7698.
(20) Deng, H.; Chen, Z.; Wołoś, A.; Konczykowski, M.; Sobczak, K.; Sitnicka, J.; Fedorchenko, I. V.; Borysiuk, J.; Heider, T.; Pluciński, Ł.; Park, K.; Georgescu, A. B.; Cano, J.; Krusin-Elbaum, L. High-Temperature Quantum Anomalous Hall Regime in a $MnBi_2Te_4/Bi_2Te_3$ Superlattice. *Nat. Phys.* **2021**, *17*, 36−42.
(21) Yang, S.; Xu, X.; Zhu, Y.; Niu, R.; Xu, C.; Peng, Y.; Cheng, X.; Jia, X.; Huang, Y.; Xu, X.; Lu, J.; Ye, Y. Odd-Even Layer-Number Effect and Layer-Dependent Magnetic Phase Diagrams in10.1103/PhysRevX.11.011003 $MnBi_2Te_4$. *Phys. Rev. X* **2021**, *11*, 011003.
(22) Liu, C.; Wang, Y.; Li, H.; Wu, Y.; Li, Y.; Li, J.; He, K.; Xu, Y.; Zhang, J.; Wang, Y. Robust Axion Insulator and Chern Insulator Phases in a Two-Dimensional Antiferromagnetic Topological Insulator. *Nat. Mater.* **2020**, *19*, 522−527.
(23) Sass, P. M.; Kim, J.; Vanderbilt, D.; Yan, J.; Wu, W. Robust A -Type Order and Spin-Flop Transition on the Surface of the Antiferromagnetic Topological Insulator $MnBi_2Te_4$. *Phys. Rev. Lett.* **2020**, *125*, 037201.
(24) Otrokov, M. M.; Klimovskikh, I. I.; Bentmann, H.; Estyunin, D.; Zeugner, A.; Aliev, Z. S.; Gaß, S.; Wolter, A. U. B.; Koroleva, A. V.; Shikin, A. M.; Blanco-Rey, M.; Hoffmann, M.; Rusinov, I. P.; Vyazovskaya, A. Yu.; Eremeev, S. V.; Koroteev, Yu. M.; Kuznetsov, V. M.; Freyse, F.; Sánchez-Barriga, J.; Amiraslanov, I. R.; Babanly, M. B.; Mamedov, N. T.; Abdullayev, N. A.; Zverev, V. N.; Alfonsov, A.; Kataev, V.; Büchner, B.; Schwier, E. F.; Kumar, S.; Kimura, A.; Petaccia, L.; Di Santo, G.; Vidal, R. C.; Schatz, S.; Kißner, K.; Ünzelmann, M.; Min, C. H.; Moser, S.; Peixoto, T. R. F.; Reinert, F.; Ernst, A.; Echenique, P. M.; Isaeva, A.; Chulkov, E. V. Prediction and Observation of an Antiferromagnetic Topological Insulator. *Nature* **2019**, *576*, 416−422.
(25) Yan, J.-Q.; Liu, Y. H.; Parker, D. S.; Wu, Y.; Aczel, A. A.; Matsuda, M.; McGuire, M. A.; Sales, B. C. A-Type Antiferromagnetic Order in $MnBi_4Te_7$ and $MnBi_6Te_{10}$ Single Crystals. *Phys. Rev. Mater.* **2020**, *4*, 054202.
(26) Rienks, E. D. L.; Wimmer, S.; Sánchez-Barriga, J.; Caha, O.; Mandal, P. S.; Růžička, J.; Ney, A.; Steiner, H.; Volobuev, V. V.; Groiss, H.; Albu, M.; Kothleitner, G.; Michalička, J.; Khan, S. A.; Minár, J.; Ebert, H.; Bauer, G.; Freyse, F.; Varykhalov, A.; Rader, O.; Springholz, G. Large Magnetic Gap at the Dirac Point in $Bi_2Te_3/MnBi_2Te_4$ Heterostructures. *Nature* **2019**, *576*, 423−428.
(27) Hu, C.; Tanatar, M. A.; Prozorov, R.; Ni, N. Unusual Dynamic Susceptibility Arising from Soft Ferromagnetic Domains in $MnBi_8Te_{13}$ and Sb-Doped $MnBi_{2n}Te_{3n+1}$ (n = 2, 3). *J. Phys. Appl. Phys.* **2022**, *55*, 054003.
(28) Choe, J.; Lujan, D.; Rodriguez-Vega, M.; Ye, Z.; Leonardo, A.; Quan, J.; Nunley, T. N.; Chang, L.-J.; Lee, S.-F.; Yan, J.; Fiete, G. A.; He, R.; Li, X. Electron-Phonon and Spin-Lattice Coupling in Atomically Thin Layers of $MnBi_2Te_4$. *Nano Lett.* **2021**, *21*, 6139−6145.
(29) Padmanabhan, H.; Poore, M.; Kim, P. K.; Koocher, N. Z.; Stoica, V. A.; Puggioni, D.; Wang, H.; Shen, X.; Reid, A. H.; Gu, M.; Wetherington, M.; Lee, S. H.; Schaller, R. D.; Mao, Z.; Lindenberg, A. M.; Wang, X.; Rondinelli, J. M.; Averitt, R. D.; Gopalan, V. Interlayer Magnetophononic Coupling in $MnBi_2Te_4$. *Nat. Commun.* **2022**, *13*, 1929.
(30) Degen, C. L.; Reinhard, F.; Cappellaro, P. Quantum Sensing. *Rev. Mod. Phys.* **2017**, *89*, 035002.
(31) Thiel, L.; Wang, Z.; Tschudin, M. A.; Rohner, D.; Gutiérrez-Lezama, I.; Ubrig, N.; Gibertini, M.; Giannini, E.; Morpurgo, A. F.; Maletinsky, P. Probing Magnetism in 2D Materials at the Nanoscale with Single-Spin Microscopy. *Science* **2019**, *364*, 973−976.
(32) Pelliccione, M.; Jenkins, A.; Ovartchaiyapong, P.; Reetz, C.; Emmanouilidou, E.; Ni, N.; Bleszynski Jayich, A. C. Scanned Probe Imaging of Nanoscale Magnetism at Cryogenic Temperatures with a Single-Spin Quantum Sensor. *Nat. Nanotechnol.* **2016**, *11*, 700−705.
(33) Lenz, T.; Chatzidrosos, G.; Wang, Z.; Bougas, L.; Dumeige, Y.; Wickenbrock, A.; Kerber, N.; Zázvorka, J.; Kammerbauer, F.; Kläui, M.; Kazi, Z.; Fu, K.-M. C.; Itoh, K. M.; Watanabe, H.; Budker, D. Imaging Topological Spin Structures Using Light-Polarization and Magnetic Microscopy. *Phys. Rev. Appl.* **2021**, *15*, 024040.
(34) McLaughlin, N. J.; Wang, H.; Huang, M.; Lee-Wong, E.; Hu, L.; Lu, H.; Yan, G. Q.; Gu, G.; Wu, C.; You, Y.-Z.; Du, C. R. Strong Correlation Between Superconductivity and Ferromagnetism in an Fe-Chalcogenide Superconductor. *Nano Lett.* **2021**, *21*, 7277−7283.
(35) Tetienne, J.-P.; Dontschuk, N.; Broadway, D. A.; Stacey, A.; Simpson, D. A.; Hollenberg, L. C. L. Quantum Imaging of Current Flow in Graphene. *Sci. Adv.* **2017**, *3*, No. e1602429.
(36) Ku, M. J. H.; Zhou, T. X.; Li, Q.; Shin, Y. J.; Shi, J. K.; Burch, C.; Anderson, L. E.; Pierce, A. T.; Xie, Y.; Hamo, A.; Vool, U.; Zhang, H.; Casola, F.; Taniguchi, T.; Watanabe, K.; Fogler, M. M.; Kim, P.; Yacoby, A.; Walsworth, R. L. Imaging Viscous Flow of the Dirac Fluid in Graphene. *Nature* **2020**, *583*, 537−541.
(37) Andersen, T. I.; Dwyer, B. L.; Sanchez-Yamagishi, J. D.; Rodriguez-Nieva, J. F.; Agarwal, K.; Watanabe, K.; Taniguchi, T.; Demler, E. A.; Kim, P.; Park, H.; Lukin, M. D. Electron-Phonon Instability in Graphene Revealed by Global and Local Noise Probes. *Science* **2019**, *364*, 154−157.
(38) Kolkowitz, S.; Safira, A.; High, A. A.; Devlin, R. C.; Choi, S.; Unterreithmeier, Q. P.; Patterson, D.; Zibrov, A. S.; Manucharyan, V. E.; Park, H.; Lukin, M. D. Probing Johnson Noise and Ballistic

Transport in Normal Metals with a Single-Spin Qubit. *Science* **2015**, *347*, 1129−1132.
(39) McCullian, B. A.; Thabt, A. M.; Gray, B. A.; Melendez, A. L.; Wolf, M. S.; Safonov, V. L.; Pelekhov, D. V.; Bhallamudi, V. P.; Page, M. R.; Hammel, P. C. Broadband Multi-Magnon Relaxometry Using a Quantum Spin Sensor for High Frequency Ferromagnetic Dynamics Sensing. *Nat. Commun.* **2020**, *11*, 5229.
(40) Finco, A.; Haykal, A.; Tanos, R.; Fabre, F.; Chouaieb, S.; Akhtar, W.; Robert-Philip, I.; Legrand, W.; Ajejas, F.; Bouzehouane, K.; Reyren, N.; Devolder, T.; Adam, J.-P.; Kim, J.-V.; Cros, V.; Jacques, V. Imaging Non-Collinear Antiferromagnetic Textures via Single Spin Relaxometry. *Nat. Commun.* **2021**, *12*, 767.
(41) Du, C.; van der Sar, T.; Zhou, T. X.; Upadhyaya, P.; Casola, F.; Zhang, H.; Onbasli, M. C.; Ross, C. A.; Walsworth, R. L.; Tserkovnyak, Y.; Yacoby, A. Control and Local Measurement of the Spin Chemical Potential in a Magnetic Insulator. *Science* **2017**, *357*, 195−198.
(42) Sun, Q.-C.; Song, T.; Anderson, E.; Brunner, A.; Förster, J.; Shalomayeva, T.; Taniguchi, T.; Watanabe, K.; Gräfe, J.; Stöhr, R.; Xu, X.; Wrachtrup, J. Magnetic Domains and Domain Wall Pinning in Atomically Thin $CrBr_3$ Revealed by Nanoscale Imaging. *Nat. Commun.* **2021**, *12*, 1989.
(43) Zhang, X.-Y.; Wang, Y.-X.; Tartaglia, T. A.; Ding, T.; Gray, M. J.; Burch, K. S.; Tafti, F.; Zhou, B. B. AC Susceptometry of 2D van Der Waals Magnets Enabled by the Coherent Control of Quantum Sensors. *PRX Quantum* **2021**, *2*, 030352.
(44) Zhang, S.; Tserkovnyak, Y. Flavors of Noise in Magnetic Weyl Semimetals. 2021, 2108.07305, arXiv; https://arxiv.org/abs/2108.07305, accessed 07−05−2022.
(45) Wang, H.; Zhang, S.; McLaughlin, N. J.; Flebus, B.; Huang, M.; Xiao, Y.; Fullerton, E. E.; Tserkovnyak, Y.; Du, C. R. Quantum Sensing of Spin Transport Properties of an Antiferromagnetic Insulator. *Sci. Adv.* **2022**, *8*, eabg8562.
(46) Flebus, B.; Tserkovnyak, Y. Quantum-Impurity Relaxometry of Magnetization Dynamics. *Phys. Rev. Lett.* **2018**, *121*, 187204.
(47) Rohner, D.; Happacher, J.; Reiser, P.; Tschudin, M. A.; Tallaire, A.; Achard, J.; Shields, B. J.; Maletinsky, P. (111)-Oriented, Single Crystal Diamond Tips for Nanoscale Scanning Probe Imaging of out-of-Plane Magnetic Fields. *Appl. Phys. Lett.* **2019**, *115* (19), 192401.
(48) Hu, C.; Gordon, K. N.; Liu, P.; Liu, J.; Zhou, X.; Hao, P.; Narayan, D.; Emmanouilidou, E.; Sun, H.; Liu, Y.; Brawer, H.; Ramirez, A. P.; Ding, L.; Cao, H.; Liu, Q.; Dessau, D.; Ni, N. A van Der Waals Antiferromagnetic Topological Insulator with Weak Interlayer Magnetic Coupling. *Nat. Commun.* **2020**, *11*, 97.
(49) Tan, A.; Labracherie, V.; Kunchur, N.; Wolter, A. U. B.; Cornejo, J.; Dufouleur, J.; Büchner, B.; Isaeva, A.; Giraud, R. Metamagnetism of Weakly Coupled Antiferromagnetic Topological Insulators. *Phys. Rev. Lett.* **2020**, *124*, 197201.
(50) Guo, J.; Wang, H.; Wang, X.; Gu, S.; Mi, S.; Hu, J.; Ji, W.; Gao, H.; Xia, T.; Cheng, Z. Coexisting Ferromagnetic-Antiferromagnetic Phase and Manipulation in Magnetic Topological Insulator $MnBi_4Te_7$. 2021, 2112.02320, arXiv; https://arxiv.org/abs/2112.02320, accessed 07−05−2022.
(51) Hu, C.; Lien, S.-W.; Feng, E.; Mackey, S.; Tien, H.-J.; Mazin, I. I.; Cao, H.; Chang, T.-R.; Ni, N. Tuning Magnetism and Band Topology through Antisite Defects in Sb-Doped $MnBi_4Te_7$. *Phys. Rev. B* **2021**, *104*, 054422.
(52) van der Sar, T.; Casola, F.; Walsworth, R.; Yacoby, A. Nanometre-Scale Probing of Spin Waves Using Single Electron Spins. *Nat. Commun.* **2015**, *6*, 7886.
(53) Fuchs, G. D.; Dobrovitski, V. V.; Toyli, D. M.; Heremans, F. J.; Awschalom, D. D. Gigahertz Dynamics of a Strongly Driven Single Quantum Spin. *Science* **2009**, *326*, 1520−1522.
(54) Flebus, B.; Tserkovnyak, Y. Entangling Distant Spin Qubits via a Magnetic Domain Wall. *Phys. Rev. B* **2019**, *99*, 140403.
(55) Brown, P. J.; Ziebeck, K. R. A.; Déportes, J.; Givord, D. Magnetic Correlation in Itinerant Magnetic Materials above T_c (Invited). *J. Appl. Phys.* **1984**, *55*, 1881−1886.
(56) Zhang, S. S.-L.; Zhang, S. Magnon Mediated Electric Current Drag Across a Ferromagnetic Insulator Layer. *Phys. Rev. Lett.* **2012**, *109*, 096603.
(57) Shen, K. Magnon Spin Relaxation and Spin Hall Effect Due to the Dipolar Interaction in Antiferromagnetic Insulators. *Phys. Rev. Lett.* **2020**, *124*, 077201.
(58) Rodriguez-Nieva, J. F.; Podolsky, D.; Demler, E. Hydrodynamic Sound Modes and Galilean Symmetry Breaking in a Magnon Fluid. *Phys. Rev. B* **2022**, *105*, 174412.
(59) Liu, J.; Balents, L. Anomalous Hall Effect and Topological Defects in Antiferromagnetic Weyl Semimetals: Mn_3Sn/Ge. *Phys. Rev. Lett.* **2017**, *119*, 087202.